Direct single-shot observation of millimeter-wave superradiance in Rydberg-Rydberg transitions

David D. Grimes,[1] Stephen L. Coy,[1] Timothy J. Barnum,[1] Yan Zhou,[2] Susanne F. Yelin,[3,4] and Robert W. Field[1,*]

[1]*Department of Chemistry, Massachusetts Institute of Technology, Cambridge, Massachusetts 02139, USA*

[2]*JILA, National Institute of Standards and Technology, Department of Physics, University of Colorado, Boulder, Colorado 80309-0440, USA*

[3]*Department of Physics, Harvard University, Cambridge, Massachusetts 02138, USA*

[4]*Department of Physics, University of Connecticut, Storrs, Connecticut 06269, USA*

(Received 13 April 2016; revised manuscript received 1 March 2017; published 12 April 2017)

We have directly detected millimeter-wave (mm-wave) free-space superradiant emission from Rydberg states (principal quantum number $n \sim 30$) of barium atoms in single-shot experiments. We trigger the cooperative effects with a weak initial pulse and detect the time-dependent amplitude and phase of the emitted radiation with single-shot sensitivity and 20 ps time resolution. This allows measurement and shot-by-shot analysis of the statistical distribution of decay rates, time delays, and time-dependent frequency shifts. Cooperative line shifts and decay rates are observed that exceed the 250 kHz Doppler width by a factor of 20 and the 50 Hz spontaneous emission rate by a factor of 10^5.

DOI: 10.1103/PhysRevA.95.043818

I. INTRODUCTION

The interaction of light and matter in dense atomic samples is one of the most fundamental problems in atomic physics. In particular, superradiance, the collective, coherent emission from an ensemble of electric dipoles, has been a topic of interest in quantum optics since the original description of the phenomenon by Dicke [1]. Any description of superradiance requires consideration of a combination of quantum electrodynamics, many-body theory, and nonlinear optics to fully describe the phenomenon in the richness of its details [2]. Aside from studies of the collective Lamb shift in single-photon superradiance [3–7], little attention beyond a mean-field model has been directed at the time-dependent behavior of the frequency of the emitted field [8,9]. The presently observed behavior contains potential insights into the many-body physics involved and has implications for applications of superradiance to quantum technologies, such as electric-field sensing [10], quantum information storage [11–14], and narrow linewidth lasers [15–18].

Transitions between Rydberg states are unique in that they can have both long wavelengths and extremely large electric dipole transition moments. This makes them uniquely well suited for the observation of collective effects at relatively low atom number densities ($\rho \sim 10^6$ cm^{-3}). For Rydberg states with $n \sim 30$, $\Delta n = 1$ transitions lie at $\sim$300 GHz ($\lambda \sim 1$ mm) and have transition moments on the order of 500 D [19]. As a result, investigations of cooperative effects in Rydberg states can sample much higher optical depths ($\mathcal{D}_{\text{opt}} = \rho\lambda^2 L \approx 10^6$, where L is the characteristic length of the sample) than Bose-Einstein condensates or ensembles of atoms trapped in a magneto-optical trap [20,21].

In previous studies, the total number of atoms in a single Rydberg state has been too small to permit direct, free-space detection of the emitted electromagnetic field in a single shot. Typical studies of collective effects in ensembles of atoms in Rydberg states have primarily relied on state-selective field ionization detection in order to infer *indirectly* that superradiance has occurred [22–25]. However, *direct* detection of the emitted electric field was achieved in cavity-based maser experiments in the 1980s. But those experiments were sensitive only to the *intensity* of the emission, not to any frequency effects due to the constraints by the cavity [26,27]. Free induction decay (FID) detected experiments have been able to detect superradiance as the leading source of homogeneous broadening [28,29] and directly observe superradiance while averaging away shot-to-shot fluctuations [30].

Recent improvements in millimeter-wave (mm-wave) technology [28,29,31–33] and atomic beam sources [30,34,35] have enabled *direct* observation of *free-space* superradiance *in a single shot*. In this paper, we report direct, frequency-resolved, heterodyne detection of the time-dependent emitted oscillating electric field that arises from superradiance in a sample of barium atoms initially prepared in a single, laser-populated initial Rydberg state. Similar to single-atom or single-molecule spectroscopy, single-shot detection of the emitted field preserves the frequency domain effects generated by shot-to-shot variations in a sample of 100% initially oriented dipoles. We observe cooperative line shifts of the emission frequency thousands of times larger than the natural decay width. Additionally, the sensitivity of the experiment allows us to observe the evolution of the sample from initial superradiant emission into long-lived, coherent, cooperative emission.

II. THEORETICAL BACKGROUND

As first considered by Dicke [1], a collection of N coherently prepared two-level systems with physical separation much smaller than a wavelength can be described as a single spin $S = N/2$ system. The evolution of this system is described classically by a vector evolving on the Bloch sphere analogous to a classical damped pendulum [2]. If the system is inverted, it remains stationary until the first spontaneous emission event occurs or an on-resonance oscillating electric field (potentially from a blackbody emitter) is encountered. This first event tilts the Bloch vector by an angle θ^i from the

*rwfield@mit.edu

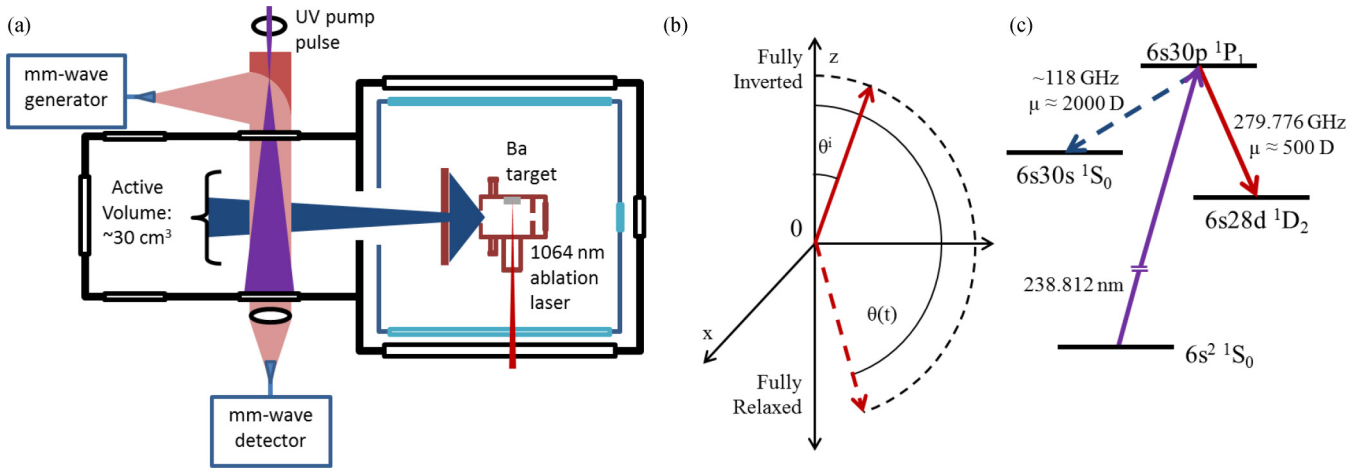

FIG. 1. (a) Schematic diagram of the experimental setup. Details of the mm-wave generation and ablation conditions are included in the text. (b) The Bloch angle formalism for describing mean-field superradiance. (c) Energy-level diagram. The dotted arrow connecting the $6s30p$ and $6s30s$ states indicates the origin of the superradiant emission is spontaneous rather than triggered.

z axis [see Fig. 1(b)] and initiates evolution according to the equations [2]

$$\frac{d\theta}{dt} = \frac{\sin[\theta(t)]}{2T_R}, \tag{1a}$$

$$\bar{N}(t) = \frac{N_u - N_l}{2} = \frac{N}{2}\cos[\theta(t)], \tag{1b}$$

$$\theta(t=0) = \theta^i, \tag{1c}$$

where θ is the angle between the Bloch vector and the z axis, $\bar{N}$ is half the difference in population between the upper (N_u) and lower (N_l) states, and T_R is the characteristic superradiance time given by [36]

$$T_R = \frac{8\pi}{\rho\lambda^2 L A_{21}}, \tag{2}$$

where A_{21} is the Einstein A coefficient for the transition. The corresponding radiated field amplitude is

$$I(t) = -\hbar\omega_0\frac{d\bar{N}}{dt} = \frac{\hbar\omega_0 N}{2T_R}\,\mathrm{sech}^2\left[\frac{1}{2T_R}(t+T_D)\right], \tag{3}$$

where T_D is the characteristic delay time given by $T_D = -2T_R\ln(\theta^i/2)$ and $\hbar\omega_0$ is the energy difference between the two states. However, these equations are correct only for a sample length much shorter than a wavelength. For extended sample geometries, as in our experiments, Eq. (3) remains a very good approximation for the evolution of the electric-field amplitude, with a correction that the characteristic evolution time changes from $2T_R$ to $4T_R$ due to interference between emission from spatially separated portions of the sample [23]. Further, these equations describe superradiance from a purely *classical* perspective, again a good approximation for the data presented in this paper. The classical theory, however, has no mechanism to describe frequency effects of superradiance, such as line shifts and line broadenings, of the sort we observe. The *quantum-mechanical* theory that can treat these effects is only recently developed [9,37]. Line shifts and line broadenings are naturally accounted for in the quantum-mechanical theory in the form of second-order correlations in the electric field generated by the superradiant sample [37]. Comparisons can currently only be made at a qualitative level as quantum-mechanical calculations for optical depths greater than $\sim 10^4$ suffer from numerical instability. For a more complete fundamental description of superradiance and cooperative effects, both classical and quantum mechanical, we refer interested readers to previous comprehensive reviews [2,9].

Ensembles of Rydberg states have a number of special features that set them apart from the noninteracting two-level systems that are typically treated theoretically. Foremost among these is the presence of strong long-range dipole-dipole interactions between emitters. These interactions are the origin of several seemingly distinct quantum many-body phenomena, such as Rydberg blockade, Förster resonances, and long-range dipole-bound states. Superradiance is another manifestation of dipole-dipole interactions, and differs from the above in that the fundamental interactions are between *transition* dipole moments [9]. These interactions could be observed in any system, but are particularly strong in ensembles of atoms in Rydberg states due to the extremely large $\Delta n = 1$ electric dipole transition moments between Rydberg states.

However, observation of superradiance in ensembles of Rydberg states can be made difficult by other broadening and dephasing mechanisms [21]. In particular, the unique signature of superradiance, namely, the initial *increase* in the radiated electric field as opposed to the usual monotonic exponential decrease of radiated electric field, can be obscured if other dephasing mechanisms operate on significantly shorter time scales than T_R. Long-range dipole-dipole mediated Rydberg-Rydberg collisions homogeneously dephase individual emitters at a rate of [38]

$$\gamma_{\mathrm{dd}} = \frac{\pi\mu^2\rho}{4\epsilon_0\hbar} \tag{4}$$

compared to a superradiant decay rate of

$$\gamma_{\mathrm{SR}} = \frac{1}{T_R} = \frac{\pi\mu^2\rho}{3\epsilon_0\hbar}\frac{L}{\lambda}. \tag{5}$$

The two rates are essentially equivalent to within a geometric factor of L/λ. For extended sample geometries, as in our experiments, $L \gg \lambda$, and the superradiant decay rate can be orders of magnitude larger than the rate of homogeneous dipole-dipole dephasing. Other Rydberg superradiance experiments that take place in, for example, magneto-optical traps [21], may sample higher absolute densities, but do not observe superradiance effects due to this competing dephasing rate. Other homogeneous dephasing factors, such as interactions of the Rydberg sample with blackbody radiation [39] and pressure broadening from collisions with neutral buffer gas atoms [40] are also significantly slower than the superradiant decay rate [29].

Inhomogeneous broadening effects can inhibit superradiance by destroying the exchange symmetry that underlies collective emission and superradiance [41]. Rydberg states in particular, due to their very large polarizabilities, can be exceptionally sensitive to inhomogeneous electric and magnetic fields, and control of these fields is discussed in the following section. Dipole-dipole interactions can introduce inhomogeneous broadening in frozen ensembles through variations in the transition frequency across the sample, and could be sampled by measuring the superradiant emission, or lack thereof.

III. EXPERIMENTAL APPARATUS AND PROCEDURE

We generate an atomic beam of barium atoms using a neon buffer gas cooled atomic beam similar to that described in Ref. [30] and summarized briefly here. Barium atoms are generated by ablation of a barium metal target inside a buffer gas cell with a 50 mJ/pulse of the 1064 nm fundamental of a Q-switched Nd:YAG laser focused to a 1 mm^2 spot size. The ablation plume of Ba atoms is entrained in a 20 SCCM (standard cubic centimeters per minute) flow of 20 K neon ($\sim$10 mTorr steady-state pressure inside the cell) and is hydrodynamically expanded into vacuum, then through a 2-cm-diameter skimmer held at 6 K, to form a loosely collimated atomic Ba beam. This beam is crossed by the laser and mm-wave pulses in a separate chamber 15 cm downstream from the ablation region. This beam has a laboratory frame velocity of 180 m/s, transverse translational temperature of 5 K, and transverse Doppler width of 250 kHz at 300 GHz. Atoms are excited into Rydberg states by pumping the $6s^2\,{}^1S_1 \rightarrow 6s30p\,{}^1P_1$ transition with a 238.812 nm, 7.5 ns laser pulse produced by the doubled output of a seeded Nd:YAG-pumped dye laser. This typically excites 3×10^8 to 1.5×10^9 total atoms into a single Rydberg state within a volume of 30 cm^3 ($1 \times 10^7 < \rho < 5 \times 10^7$ cm^{-3}) and characteristic length of 15 cm in the pencil-shaped geometry. The length of the sample is determined by the divergence of the atomic beam [42] and the cross-sectional area of the sample is determined by the beam waist of the millimeter waves of 0.75 cm. The total optical depth in this experiment is therefore (for $\lambda \sim 1$ mm) $1 \times 10^6 < \mathcal{D}_{\rm opt} < 5 \times 10^6$, due to the high density provided by the buffer gas source, and L/λ is 150, due to the large characteristic length of the system.

Immediately following excitation to the Rydberg state, a 10-ns mm-wave pulse, on resonance with the $6s30p\,{}^1P_1 \rightarrow 6s28d\,{}^1D_2$ ($A_{21} \approx 50$ Hz) transition at 279.776 GHz, triggers the superradiant emission (with the ${}^1P_1$ state as the upper state and the ${}^1D_2$ state as the lower state). This pulse is formed using a Virginia Diodes active multiplier chain (AMC) to multiply the frequency output from a 12-GS/s Agilent arbitrary waveform generator (AWG) mixed with a fixed-frequency 8.8 GHz local oscillator (LO). The mm-wave pulse energy is 0.3 pJ ($\sim$0.1 V/cm), which causes a $\theta^i = \pi/40$ initial tip angle of the Bloch vector. The time delay between initial excitation and initiation of superradiance (<10 ns) is much shorter than the typical time required for a spontaneous emission event to occur ($\sim$20 ms) or for an on-resonance blackbody photon to interact with the system ($\sim$10 μs). We take the Bloch vector tip angle to be determined entirely by this initiating mm-wave pulse. We detect the subsequent superradiant pulse at 279.776 GHz *directly in the time domain* by heterodyning against an LO set to 277.200 GHz. This radiation is generated by the same AWG and 8.8 GHz LO, using a second AMC for multiplication. The resultant output is recorded on a 50-GS/s oscilloscope. The mm-wave radiation is generated and detected in polarization-sensitive waveguide components, thus only millimeter waves of the same polarization as the source are detected.

In order to avoid creating standing waves and unintentional etalons that could modify the frequency of the superradiant emission, all mm-wave components outside the vacuum chamber are positioned with their faces tilted slightly away from normal to the propagation direction of the radiation. The largest remaining source of standing waves is the weak cavity formed between the microwave transmission and receiving horns, 90 cm apart. The largest cavity-induced fluctuations in our instrument response are on the order of 20% of the full field amplitude, indicating a cavity with finesse $\ll$1 and a negligible contribution from standing waves. Additionally, the Earth's magnetic field is compensated (to the 0.1 G level) with a set of Helmholtz coils surrounding the vacuum chamber. A stray field of 0.1 G would cause an $\sim$150 kHz Zeeman splitting, much smaller than the 250 kHz Doppler broadening.

The primary source of inhomogeneous electric fields is ions formed via multiphoton ionization of ground-state Ba atoms; multiphoton ionization is minimized by carefully reducing the amplified spontaneous emission from the pulsed dye laser (reduced below 1% of total fundamental output power). Ions formed in the ablation process and swept downstream with the rest of the ablatant could also produce an inhomogeneous electric field, and we have optimized the ablation to reduce the ion density in the active region to $<10^6$ cm^{-3}, monitored by laser-induced fluorescence spectroscopy on the Ba^+ ion $6s$-$6p$ transition, corresponding to an inhomogeneous broadening of $\sim$10 kHz, far less than the Doppler broadening. FID detection, unlike ion detection, requires no high-voltage-biased components, thus unwanted homogeneous electric fields are negligible in the interaction region.

A schematic representation of the experiment and level diagram are shown in Figs. 1(a) and 1(c). The data discussed here are from 111 single shots, of which 56 had a signal-to-noise ratio large enough to be individually fitted. The largest effect on the signal-to-noise ratio of each shot was the shot-to-shot variation in Rydberg density that results from variations in both the ablation laser intensity and the dye laser intensity.

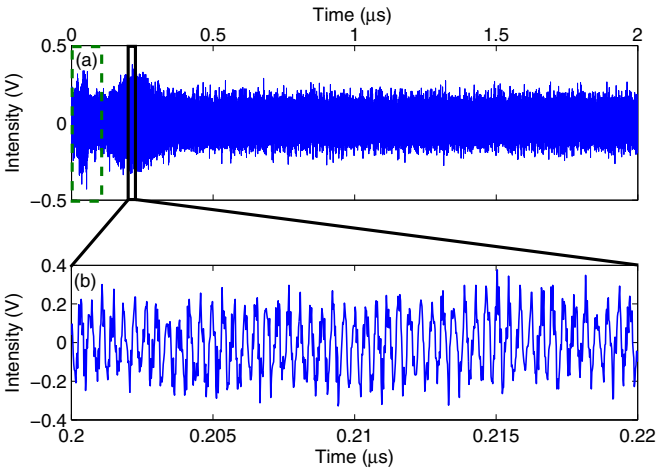

FIG. 2. (a) Raw *single-shot* data trace recorded in the experiment. The dashed-boxed feature is the tipping pulse that initiates the superradiance, and the larger feature is the superradiant emission. (b) A zoom-in of the solid-boxed portion of the raw data trace from (a).

IV. RESULTS AND ANALYSIS

An example of the raw data from the oscilloscope is shown in Fig. 2(a). The initial dashed-boxed peak is the initial mm-wave tipping pulse, while the second, larger, and broader peak is the superradiant emission. A zoom-in on the emission from the superradiant emission is displayed in Fig. 2(b). Due to our 20 GHz detection bandwidth, most of the noise is at frequencies far from the resonance frequency, thus we make use of post-experimental digital filtering methods to improve the signal-to-noise ratio. Briefly, we independently measure the resonance frequency at low density (279.776 GHz) and multiply the signal by a sine and a cosine wave at that frequency to extract, respectively, the in-phase and quadrature components of the signal. We then use a 25 MHz classic type-I finite impulse response (FIR) zero-phase low-pass filter to remove the high-frequency noise [43]. A full discussion of this filter can be found in the Appendix.

We calculate the time-dependent radiated electric-field *amplitude* and *phase* independently with $I(t) = s^2 + c^2$ and $\phi(t) = \tan^{-1}(s/c)$, where s and c are the in-phase and quadrature components of the signal. The phase is calculated using a four-quadrant arctangent function. After filtering, we fit the time-domain field amplitude to Eq. (3) in order to determine the optical depth of the sample on a shot-by-shot basis. Figure 3(a) is an example of a fitted filtered signal. The width and delay of the signal (T_R and T_D) are independently fitted simultaneously. In order to confirm that the model used to interpret the data is appropriate, we plot T_R vs T_D, and the results are shown in Fig. 4. Since $T_D = -2T_R \ln(\theta^i/2)$, we expect a linear correlation with a slope that is directly related to the initial tipping angle of the triggering pulse. The linear correlation between T_R and T_D is clear, and the tipping angle extracted from the relationship between T_R and T_D matches the independently measured value of θ^i of $\pi/40$.

Figure 3(b) shows the Fourier transform of an unfiltered signal from Fig. 2(a), gated to exclude the initial tipping pulse, and a fitted line shape. Two features are prominent. First, the

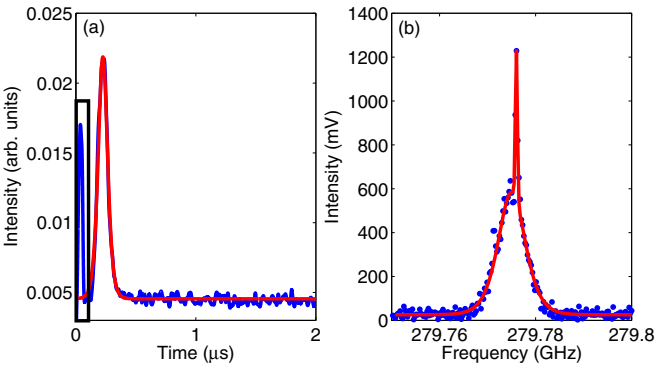

FIG. 3. (a) The digitally filtered electric-field amplitude profile is shown in blue, and the fit to the mean-field emission functional form is shown in red. The boxed feature is the tipping pulse that triggers the superradiance. (b) The Fourier transform of the raw data from (a). The blue points are the data and the red line is the fit to a sum of the two line-shape functions, as described in the text.

broad feature is the signal associated with the superradiant burst of radiation. It has a width of 6 MHz and is shifted to 2 MHz below the low-density transition frequency. The narrow feature is the signal emitted after 500 ns, which is after the superradiant evolution has concluded, with width (∼250 kHz) consistent with Doppler broadening and no observable shift from the transition frequency at low density. The fitted line shape is the sum of a narrow Gaussian peak, centered at the low-density resonance, and a hyperbolic secant peak, the center frequency of which was allowed to vary in the fit. When performing a Fourier transform with a time gate that excludes *both* the initial tipping pulse and the superradiant pulse, only the narrow feature remained. An intentional decrease of the sample density leads to a matched amplitude reduction of both broad and narrow signals, indicating that the narrow feature is fully cooperative in nature, rather than having been

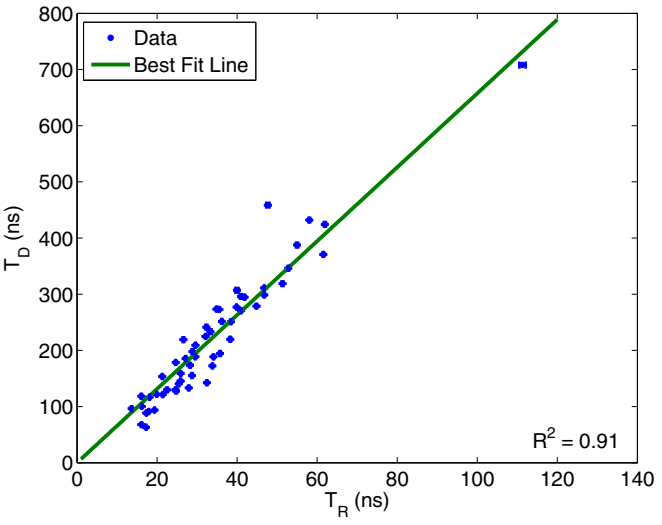

FIG. 4. Relationship between the separate fitting parameters T_R (characteristic superradiance emission time) and T_D (superradiance delay time). Blue points are the data and the green line is the best fit to the data. Error bars represent 95% confidence intervals.

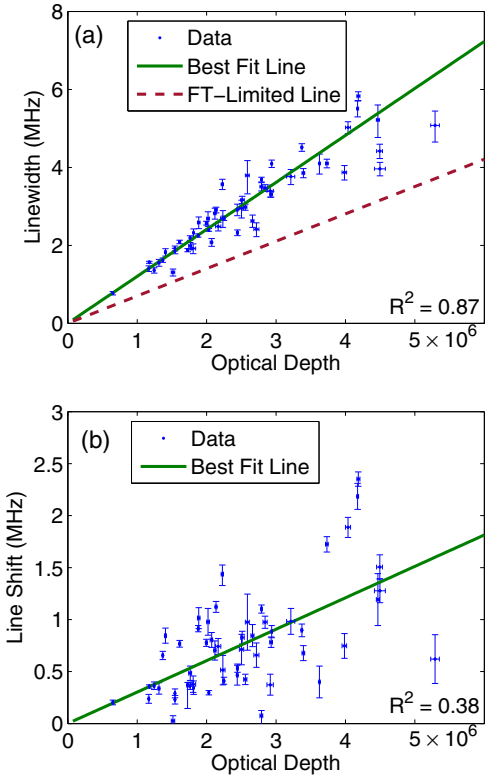

FIG. 5. (a) Observed relationship between the optical depth of a superradiant sample and the linewidth of the emitted radiation. Blue points are the data, the green line is the best fit to the data, and the red dashed line is the expected linewidth if the emission were Fourier-transform limited. Error bars represent 95% confidence intervals. (b) Observed relationship between the optical depth of a superradiant sample and the frequency shift. Blue points are the data and the green line is the best fit to the data. Error bars represent 95% confidence intervals.

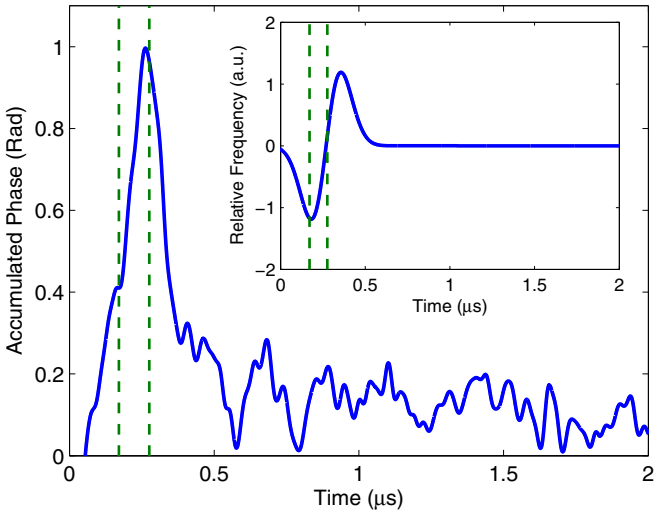

FIG. 6. The recorded phase as a function of time, obtained by demodulation at the low-density resonance frequency. The green dashed lines indicate the FWHM of the superradiant emission field amplitude. A positive slope indicates a frequency that is shifted lower than the resonance frequency, while a negative slope indicates a shift to higher than the resonance frequency. The inset shows a fitted frequency evolution associated with the displayed phase evolution, as explained in the text, and the green dashed lines in the inset indicate the FWHM of the superradiant emission amplitude. The low-density resonance frequency is taken as zero.

generated in low-density portions of the sample. However, this emission from low-density regions cannot be ruled out. We defer assignment of the source of this signal to a following paper.

The shot-to-shot variation in the number of excited atoms permits observation of the optical depth dependence of the frequency width and shift, using the optical depth as determined from time-domain fits of T_R using Eq. (3). The width of the superradiant feature varies linearly (fitting quality $R^2 = 0.87$) with optical depth, as shown in Fig. 5(a). This is expected, as T_R is inversely proportional to optical depth. However, the width is consistently larger than the Fourier-transform-limited linewidth of a time-domain hyperbolic secant signal with characteristic width T_R. In Fig. 5(a), the solid green line is the result of a linear fit of the optical depth vs linewidth, while the dashed red line displays what the width would be if it were Fourier-transform limited. The observed excess frequency width could be due to either a frequency chirp during the emission process, or a dephasing process (e.g., inhomogeneous dipole-dipole broadening). Since we directly detect the emitted electric-field amplitude in the time domain, any dephasing process would have been immediately apparent as a shortening of the emitted superradiant pulse due to destructive interference. Therefore, the excess width implicates a frequency chirp across the linewidth of the emission feature.

This chirp is most directly measured by observing the accumulated phase of the emitted radiation, because the instantaneous frequency is determined by the time derivative of the phase. The accumulated phase is directly sampled by our methods of detection and filtering. The blue solid trace in Fig. 6 displays the phase evolution of the single-shot data trace in Fig. 2(a). In the absence of a model for the frequency and hence the phase evolution of the sample, the phase evolution was fit to a series of line-shape functions (Gaussian, Lorentzian, hyperbolic secant) and the derivative of each was computed in order to determine the frequency as a function of time. Qualitatively, each line-shape fit model produced the same results. The frequency evolution determined from the Gaussian fit is shown in the inset to Fig. 6, plotted relative to the low-density emission frequency. The previously discussed frequency chirp implied by the excess frequency-domain width is clearly present. Additionally, the time at which the maximum in the phase evolution occurs and the frequency crosses through the low-density resonance frequency does not coincide with the envelope of the field amplitude in the time domain. The FWHM of the superradiant emission amplitude is displayed by the green dashed lines in Fig. 6 to demonstrate this offset. This mismatch between the phase evolution and the electric-field envelope causes the frequency shift observed in the frequency domain. This is because the emission is most intense while the frequency is shifted away from the low-density value, despite the fact that the chirp is symmetric around the low-density frequency. In a fully quantum-mechanical many-body

treatment, as in [9,37], both a chirp and an overall shift to lower frequencies are predicted during the maximum amplitude of the superradiant emission. These calculations predict a large redshift during the peak amplitude of the superradiant emission that chirps toward a long-lived blueshift at long times, in qualitative agreement with our observations. Comparisons can only be made at a qualitative level due to the vastly larger optical depth in our experiment than is currently tractable in simulations.

It was not possible to establish a relationship between Rydberg optical depth and the observed frequency shift in this work. Quantum many-body calculations indicate that the induced superradiant line shift depends predominantly on the relative density ($\mathcal{D}_{\rm rel} = \rho\lambda^3 = \mathcal{D}_{\rm opt}\lambda/L$) instead of the optical depth [37]. The $6s30s\,^1S_0$ state lies $\sim$4 cm^{-1} below the $6s30p\,^1P_1$ state, as shown in Fig. 1(b), and the $6s30p$ state decays superradiantly to the $6s30s$ state *without* a trigger pulse. This population decay is triggered by a blackbody photon (or a much rarer spontaneous emission event), and originates both at a random location in the atomic sample and at an uncontrolled time in the experiment. Therefore, the spatial distribution of emitters taking part in the triggered superradiance changes on a shot-by-shot basis, as does the length of the sample and all propagation effects. This partitioning between triggered and untriggered superradiance makes it impossible to establish a quantitative relationship between number density, geometry, and frequency shift. Our data show that there is only a weak dependence ($R^2 = 0.38$) of frequency shift on optical depth, as shown in Fig. 5(b) which indicates the cooperative nature of the shift, but that a quantity other than optical depth controls the exact value of the frequency shift.

V. CONCLUSION

We have directly observed the time dependence of the mm-wave superradiant emitted electric field from an extended free-space sample of Rydberg atoms, including the time-dependent phase and frequency responses of our highly cooperative system. The relatively long wavelength and large electric dipole transition moments associated with Rydberg-Rydberg transitions allows for the generation of a 100% oriented dipolar gas with an extremely large optical depth, while the absence of a cavity in the system allows observation of both a frequency *chirp* and an overall frequency *shift* of the superradiant signal by $\sim 10^5$ times its natural linewidth. Additionally, after the superradiant emission, we observe long-lived, coherent emission, the source of which remains to be determined.

Further work is necessary, both experimentally and theoretically, to more completely describe both the frequency effects and the source of the long-lived emission. Shot-to-shot geometry variations due to uncontrolled superradiance are the primary limiting factor in the experiment. These variations can be minimized by exciting directly to an ns Rydberg state and investigating the superradiant emission generated to a single $n'p$ state. With the fluctuations reduced, the relationships between the induced superradiant line shift and experimental parameters can be accurately determined, and a more in-depth time-dependent analysis of the long-lived radiation can be carried out. Multiphoton excitation schemes to access ns Rydberg states also permit careful shaping of the active experimental volume, which would permit separation of the effects of optical depth and relative density on the induced superradiant line shift. Our use of heterodyne-detected mm-wave transitions between Rydberg states provides a method with high tunability of relevant parameters (optical depth, characteristic system size, dipole-dipole coupling, etc.), which is capable of fully sampling the quantum many-body effects shown here in different parameter regimes.

ACKNOWLEDGMENTS

We thank Prof. Edward Eyler, Prof. John Muenter, and Dr. Tony Colombo for valuable comments and feedback, Professor Brooks Pate for the mm-wave spectrometer, and Gray Putnam for discussions. This material is based upon work supported by the National Science Foundation under Grants No. CHE-1361865 and No. PHY-1607637. D.D.G. was supported by the Department of Defense (DoD) through the National Defense Science & Engineering Graduate Fellowship (NDSEG) Program. T.J.B. was supported by a National Science Foundation Graduate Research Fellowship under Grant No. 1122374. S.F.Y. received support for this work through the CUA PFC.

APPENDIX: ZERO-PHASE FILTERING IN A ROTATING FRAME

The electric field that reaches the detector is generated jointly by the mm-wave source and by the sample. It contains the effects of emission and absorption from many transitions in the sample including those directly excited by the radiation and radiation from levels populated by one or more cascade transitions. A number of these separate transitions can occur within the bandwidth of our detection system, but others are not detected. We have identified the strongest transitions within our detection bandwidth and want to restrict our observations to the signals from directly excited transitions. These are most clearly represented when referred to a rotating frame at a frequency near the natural transition frequency and when the noise from remote frequency elements is eliminated using a narrow-bandwidth filter that preserves the transition dynamics.

The superradiance dynamics of a particular transition is detected by two linked rotating-frame transformations. The first step is done in hardware through heterodyne detection in a subharmonically pumped mixer which produces a signal proportional to the product of the electric field from the sample (rf) and a local oscillator (LO) generated by frequency multiplication in the mixer. The second step is a dual-phase rotating-frame transformation in software that is specific to the frequency of a selected transition in the hardware bandwidth. The software transformation consists of dual-phase mixing with a demodulation waveform (D) at frequency ω_D. The excess noise is then removed by a phase-linear low-pass filter with a bandwidth on the order of tens of megahertz chosen for fidelity to the observed dynamics. The combined steps allow faithful recovery of a signal proportional to the electric field that reaches the detector from the selected transition. It is computed in a rotating frame at the combined LO+D

frequencies with a phase reference that is known relative to the applied exciting mm-wave electric field [30].

At each rotating-frame transformation, high-frequency terms are discarded in the rotating-wave approximation. For the first rotating-frame transformation, the voltage output from the subharmonic mixer is

$$\begin{aligned} E_1(t) &= \langle E_{\rm LO}(t) E_{\rm rf}(t)\rangle \\ &= \tfrac{1}{2} S_{\rm LO} S_{\rm rf}(t) \cos[\phi_{\rm rf}(t) - \phi_{\rm LO}(t)] \\ &= \tfrac{1}{2} S_{\rm LO} S_{\rm rf}(t) \cos[\phi_1(t)]. \end{aligned} \tag{A1}$$

The LO and rf electric fields contain constant or slowly varying electric-field amplitudes $S_{\rm LO}$ and $S_{\rm rf}(t)$, with frequency and phase factors:

$$E_{\rm LO}(t) = S_{\rm LO} \sin[\phi_{\rm LO}(t)], \tag{A2a}$$

$$\phi_{\rm LO}(t) = \omega_{\rm LO} t - \zeta_{\rm LO}, \tag{A2b}$$

$$E_{\rm rf}(t) = S_{\rm rf}(t) \sin[\phi_{\rm rf}(t)], \tag{A2c}$$

$$\phi_{\rm rf}(t) = \omega_{\rm rf} t - \zeta_{\rm rf}, \tag{A2d}$$

$$\phi_1(t) = \phi_{\rm rf}(t) - \phi_{\rm LO}(t). \tag{A2e}$$

The phases $\phi_{\rm LO}(t), \phi_{\rm rf}(t)$ are defined at the detector location so the spatial dependence is omitted, as is the atomic speed dependence, which generates the Doppler effect. The LO is constant in frequency and $\zeta_{\rm LO}$ is a constant phase offset. For the rf field, only $\phi_{\rm rf}(t)$ is observed, so we choose to allow the frequency to vary during the emission, while the rf reference phase $\zeta_{\rm rf}$ is a constant that can be determined from the signal at a specified time that is a characteristic of the experimental setup. $E_1(t)$ can only be detected within the intermediate frequency output bandwidth of our mixer-preamp-oscilloscope system (18 GHz, digitized at 20 ps steps). Detection is in double-sideband (DSB) mode (detects both sides of LO) so there is an ambiguity in rf frequency which is resolved by varying the LO frequency or by approximate knowledge of the rf. DSB detection results in 3 dB excess noise at each frequency from the matching sideband, but in compensation the detection system is free of complexity, and the effective frequency coverage is doubled. Since both phase and frequency information are available in $E_1(t)$, while the LO and rf are ultimately derived from the same stable clock, and the sign of the rf-LO difference frequency is known, the rf field is constructible from $E_1(t)$. $E_1(t)$ is digitized by the fast oscilloscope in 20 ps steps, corresponding to a Nyquist rate of 25 GHz.

The second rotating-frame transformation to the frequency of one selected transition in $E_1(t)$ is performed in software by selecting low-frequency terms after convolving with a demodulation sinusoid (D). Both sine and cosine are used, to maintain signal-to-noise quality and most clearly preserve phase information.

$$E_{2c}(t) = \langle E_1(t) \cos[\phi_D(t)]\rangle = \frac{S_{\rm LO}}{4} S_{\rm rf}(t) \cos[\omega_\Delta(t) - \zeta_\Delta], \tag{A3a}$$

$$E_{2s}(t) = \langle E_1(t) \sin[\phi_D(t)]\rangle = -\frac{S_{\rm LO}}{4} S_{\rm rf}(t) \sin[\omega_\Delta(t) - \zeta_\Delta], \tag{A3b}$$

where the phase and frequency terms above are defined by

$$\omega_D \cong \omega_{\rm rf}(t) - \omega_{\rm LO}, \tag{A4a}$$

$$\phi_D(t) = \omega_D t, \tag{A4b}$$

$$\omega_\Delta(t) = \omega_{\rm rf}(t) - \omega_{\rm LO} - \omega_D, \tag{A4c}$$

$$\zeta_\Delta = \zeta_{\rm rf} - \zeta_{\rm LO}, \tag{A4d}$$

and where $\omega_\Delta(t) \approx \omega_D$. The frequency scale in the E_2 terms is centered at the transition frequency but they are computed on the same very fine time grid as E_1 (20 ps interval, Nyquist frequency 25 GHz) and contain noise from the entire 18 GHz bandwidth.

To reduce noise and smooth the time resolution, a classic type-I FIR low-pass filter is used [43]. FIR filters are implemented by a convolution of the time sequence with a fixed bank of coefficients. The single-pass nature of the filter results in a fixed time delay from signal to output, and an effective degradation in time resolution. These filters are described as phase linear; the constant time delay is equivalent to a linearly increasing phase delay as a function of bandpass frequency. Different frequencies are differently attenuated, but the time delay is independent of frequency, so the signal is smoothed but not distorted.

There are two parameters in a type-I FIR low-pass filter: (1) cutoff frequency as a fraction of the Nyquist rate ($g_{\rm lp}$) and (2) filter order, $N_{\rm lp}$ (number of coefficients is $N_{\rm lp} + 1$). The filter order determines the degree of sidelobe suppression. Choosing the filter order to be an even number makes the time delay an even number of time steps. We choose the filter order as

$$N_{\rm lp} = 2\left\lceil \frac{1}{2 g_{\rm lp}} \right\rceil, \quad g_{\rm lp} = \frac{\nu_{\rm lp}}{\nu_{Nyq}}, \quad \nu_{Nyq} = \frac{1}{2 t_{\rm step}}. \tag{A5}$$

The number of points which depend on unknown values before or after the available data, and thus should be deleted from the output, is $N_{\rm lp}/2$ for a single-pass type-I FIR filter.

To eliminate the time delay of a linear phase FIR filter, a zero-phase double-pass implementation can be used. On the saved data stream, the FIR filter is applied forward and then

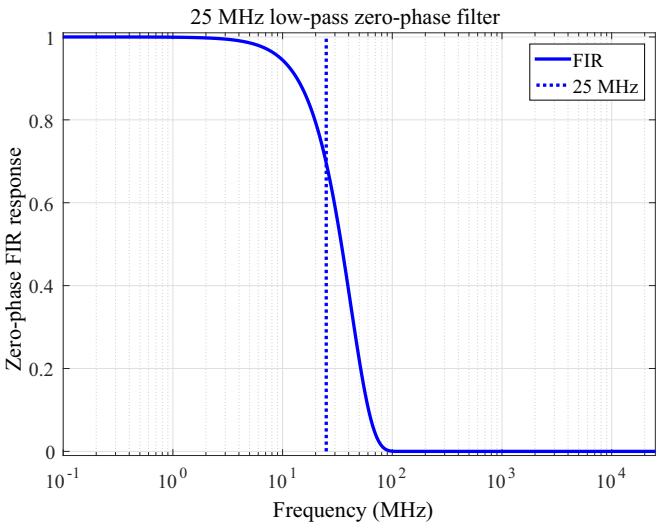

FIG. 7. Frequency response of a typical 25 MHz zero-phase filter.

backward. The result is an output which remains perfectly aligned with the original time scale. For the forward-backward zero-phase filter, the suppression ratio of spurious features in the stop band is squared (doubled in dB terms) while the ripple in the passband is negligibly affected. The cost involved in this convenient usage is a doubling of the size of the compact support of the filter, requiring that N_{lp} points be omitted from the output.

As an example of a typical filter applicable to superradiant features following the excitation pulse, we show the frequency response of a 25 MHz zero-phase filter in Fig. 7. With $\nu_{\mathrm{lp}} = 25$ MHz, $t_{\mathrm{step}} = 20$ ps, $\nu_{\mathrm{Nyq}} = 25$ GHz, then $g_{\mathrm{lp}} = 0.001$, $N_{\mathrm{lp}} = 1000$. The time span that must be deleted from the beginning and end of the data is then 40 ns, compared to a full data sample of 4 μs. Since the mm-wave level is zero before the excitation pulse, the pretrigger data can be zero-filled to minimize the importance of the initial delay. Stop-band suppression for commercial zero-phase filters with the filter order given in Eq. (A5) is better than 10^{-5}. These filtering methods are available in MATLAB, using *fir1* for filter design, *filter* and *filtfilt* for linear-phase and zero-phase filtering, and *freqz* for the computation of the frequency and phase response.

[1] R. H. Dicke, Phys. Rev. **93**, 99 (1954).
[2] M. Gross and S. Haroche, Phys. Rep. **93**, 301 (1982).
[3] M. O. Scully, Phys. Rev. Lett. **102**, 143601 (2009).
[4] R. Rohlsberger, K. Schalge, B. Sahoo, S. Couet, and R. Ruffer, Science **328**, 1248 (2010).
[5] J. Javanainen, J. Ruostekoski, Y. Li, and S. M. Yoo, Phys. Rev. Lett. **112**, 113603 (2014).
[6] S. J. Roof, K. J. Kemp, M. D. Havey, and I. M. Sokolov, Phys. Rev. Lett. **117**, 073003 (2016).
[7] M. O. Araújo, I. Krešić, R. Kaiser, and W. Guerin, Phys. Rev. Lett. **117**, 073002 (2016).
[8] J. MacGillivray and M. Feld, Phys. Rev. A **14**, 1169 (1976).
[9] G.-D. Lin and S. F. Yelin, *Advances in Atomic, Molecular, and Optical Physics* (Elsevier, New York, 2012), Vol. 61, pp. 295–329.
[10] J. Kitching, S. Knappe, and E. A. Donley, IEEE Sens. J. **11**, 1749 (2011).
[11] J. P. Clemens, L. Horvath, B. C. Sanders, and H. J. Carmichael, Phys. Rev. A **68**, 023809 (2003).
[12] A. T. Black, J. K. Thompson, and V. Vuletić, Phys. Rev. Lett. **95**, 133601 (2005).
[13] A. A. Svidzinsky, J. T. Chang, and M. O. Scully, Phys. Rev. A **81**, 053821 (2010).
[14] M. O. Scully, Phys. Rev. Lett. **115**, 243602 (2015).
[15] D. Meiser, J. Ye, D. R. Carlson, and M. J. Holland, Phys. Rev. Lett. **102**, 163601 (2009).
[16] J. G. Bohnet, Z. Chen, J. M. Weiner, D. Meiser, M. J. Holland, and J. K. Thompson, Nature (London) **484**, 78 (2012).
[17] J. G. Bohnet, Z. Chen, J. M. Weiner, K. C. Cox, and J. K. Thompson, Phys. Rev. Lett. **109**, 253602 (2012).
[18] A. A. Svidzinsky, L. Yuan, and M. O. Scully, Phys. Rev. X **3**, 041001 (2013).
[19] $1\ \mathrm{D} = 3.336 \times 10^{-30}\ \mathrm{C\,m} = 0.393\, e\, a_0$.
[20] S. L. Bromley, B. Zhu, M. Bishof, X. Zhang, T. Bothwell, J. Schachenmayer, T. L. Nicholson, R. Kaiser, S. F. Yelin, M. D. Lukin, A. M. Rey, and J. Ye, Nat. Commun. **7**, 11039 (2016).
[21] T. Zhou, B. G. Richards, and R. R. Jones, Phys. Rev. A **93**, 033407 (2016).
[22] M. Gross, P. Goy, C. Fabre, S. Haroche, and J. M. Raimond, Phys. Rev. Lett. **43**, 343 (1979).
[23] L. Moi, P. Goy, M. Gross, J. M. Raimond, C. Fabre, and S. Haroche, Phys. Rev. A **27**, 2043 (1983).
[24] T. Wang, S. F. Yelin, R. Côté, E. E. Eyler, S. M. Farooqi, P. L. Gould, M. Koštrun, D. Tong, and D. Vrinceanu, Phys. Rev. A **75**, 033802 (2007).
[25] J. Han and H. Maeda, Can. J. Phys. **1134**, 1130 (2014).
[26] L. Moi, C. Fabre, P. Goy, M. Gross, S. Haroche, P. Encrenaz, G. Beaudin, and B. Lazareff, Opt. Commun. **33**, 47 (1980).
[27] P. Goy, L. Moi, M. Gross, J. M. Raimond, C. Fabre, and S. Haroche, Phys. Rev. A **27**, 2065 (1983).
[28] K. Prozument, A. P. Colombo, Y. Zhou, G. B. Park, V. S. Petrović, S. L. Coy, and R. W. Field, Phys. Rev. Lett. **107**, 143001 (2011).
[29] A. P. Colombo, Y. Zhou, K. Prozument, S. L. Coy, and R. W. Field, J. Chem. Phys. **138**, 014301 (2013).
[30] Y. Zhou, D. D. Grimes, T. J. Barnum, D. Patterson, S. L. Coy, E. Klein, J. S. Muenter, and R. W. Field, Chem. Phys. Lett. **640**, 124 (2015).
[31] G. G. Brown, B. C. Dian, K. O. Douglass, S. M. Geyer, S. T. Shipman, and B. H. Pate, Rev. Sci. Instrum. **79**, 053103 (2008).
[32] B. C. Dian, G. G. Brown, K. O. Douglass, and B. H. Pate, Science **320**, 924 (2008).
[33] G. B. Park, A. H. Steeves, K. Kuyanov-Prozument, J. L. Neill, and R. W. Field, J. Chem. Phys. **135**, 024202 (2011).
[34] S. E. Maxwell, N. Brahms, R. deCarvalho, D. R. Glenn, J. S. Helton, S. V. Nguyen, D. Patterson, J. Petricka, D. DeMille, and J. M. Doyle, Phys. Rev. Lett. **95**, 173201 (2005).
[35] D. Patterson, J. Rasmussen, and J. M. Doyle, New J. Phys. **11**, 055018 (2009).
[36] N. Skribanowitz, I. P. Herman, J. C. MacGillivray, and M. S. Feld, Phys. Rev. Lett. **30**, 309 (1973).
[37] G. Putnam, G.-D. Lin, and S. Yelin, arXiv:1612.04477 .
[38] V. M. Akulin and N. V. Karlov, *Texts and Monographs in Physics* (Springer-Verlag, 1992).
[39] T. F. Gallagher, *Rydberg Atoms* (Cambridge University Press, 1994).
[40] I. L. Beigman and V. S. Lebedev, Phys. Rep. **250**, 95 (1995).
[41] V. V. Temnov and U. Woggon, Phys. Rev. Lett. **95**, 243602 (2005).
[42] N. R. Hutzler, H. I. Lu, and J. M. Doyle, Chem. Rev. **112**, 4803 (2012).
[43] A. Oppenheim, R. Shafer, and J. Buck, *Discrete-Time Signal Processing*, 2nd ed. (Prentice Hall, 1999).